JOURNAL OF SYNCHROTRON RADIATION

ISSN 1600-5775

The 3D characteristics of post-traumatic syringomyelia in a rat model: a propagation-based synchrotron radiation microtomography study

Shenghui Liao,[a]‡ Shuangfei Ni,[b,c]‡ Yong Cao,[b,c]‡ Xianzhen Yin,[d] Tianding Wu,[b,c]* Hongbin Lu,[c,e] Jianzhong Hu,[b,c] Hao Wu[b] and Ye Lang[b]

[a]School of Information Science and Engineering, Central South University, Changsha 410008, People's Republic of China, [b]Department of Spine Surgery, Xiangya Hospital, Central South University, Changsha 410008, People's Republic of China, [c]Key Laboratory of Organ Injury, Aging and Regenerative Medicine of Hunan Province, Changsha 410008, People's Republic of China, [d]Center for Drug Delivery System, Shanghai Institute of Materia Medica, Chinese Academy of Sciences, Shanghai 201203, People's Republic of China, and [e]Department of Sports Medicine, Research Centre of Sports Medicine, Xiangya Hospital, Central South University, Changsha 410008, People's Republic of China.
*Correspondence e-mail: tiandingwu@hotmail.com

Received 19 January 2017
Accepted 30 July 2017

Edited by Y. Amemiya, University of Tokyo, Japan

‡ These three authors contributed equally to this work.

Keywords: post-traumatic syringomyelia; three-dimensional; propagation-based synchrotron radiation microtomography; spinal cord injury; phase-contrast tomography.

Many published literature sources have described the histopathological characteristics of post-traumatic syringomyelia (PTS). However, three-dimensional (3D) visualization studies of PTS have been limited due to the lack of reliable 3D imaging techniques. In this study, the imaging efficiency of propagation-based synchrotron radiation microtomography (PB-SRμCT) was determined to detect the 3D morphology of the cavity and surrounding microvasculature network in a rat model of PTS. The rat model of PTS was established using the infinite horizon impactor to produce spinal cord injury (SCI), followed by a subarachnoid injection of kaolin to produce arachnoiditis. PB-SRμCT imaging and histological examination, as well as fluorescence staining, were conducted on the animals at the tenth week after SCI. The 3D morphology of the cystic cavity was vividly visualized using PB-SRμCT imaging. The quantitative parameters analyzed by PB-SRμCT, including the lesion and spared spinal cord tissue area, the minimum and maximum diameters in the cystic cavity, and cavity volume, were largely consistent with the results of the histological assessment. Moreover, the 3D morphology of the cavity and surrounding angioarchitecture could be simultaneously detected on the PB-SRμCT images. This study demonstrated that high-resolution PB-SRμCT could be used for the 3D visualization of trauma-induced spinal cord cavities and provides valuable quantitative data for cavity characterization. PB-SRμCT could be used as a reliable imaging technique and offers a novel platform for tracking cavity formation and morphological changes in an experimental animal model of PTS.

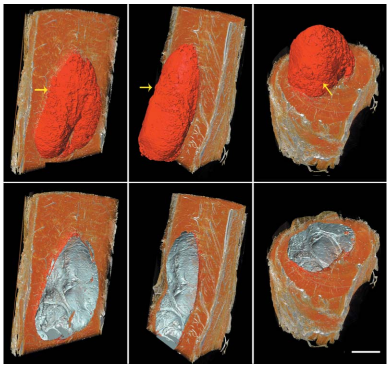

1. Introduction

Post-traumatic syringomyelia (PTS) refers to the development and progression of cerebrospinal-fluid-filled cystic cavities within the spinal cord that can cause serious neurological deterioration (Asano *et al.*, 1996; Shields *et al.*, 2012). A retrospective study has reported that approximately 7.3% of patients ultimately develop PTS following traumatic spinal cord injury (SCI), and this value will inevitably increase with time (Ko *et al.*, 2012). As the cystic cavity enlarges and extends, it causes injury to the surrounding neurological tissue. This injury is clinically characterized by the insidious progression of pain and loss of sensorimotor function (Krebs *et al.*, 2016). Factors related to cystic cavity formation include mechanical damage caused by spinal cord compression,

https://doi.org/10.1107/S1600577517011201

arterial or venous obstruction, liquefaction of an intraparenchymal hematoma, ischemia due to tethering, and release of intracellular lysosomal enzymes and excitatory amino acids (Brodbelt *et al.*, 2003*a*,*b*; Kobayashi *et al.*, 2012; Tu *et al.*, 2011; Bilston *et al.*, 2010). Because the pathophysiology of PTS has not been fully elucidated, the current treatment options do not provide satisfactory therapeutic results, and most patients fail to exhibit improvement in neurological symptoms.

A study using T2-weighted MRI images to investigate PTS and identify a syrinx in rats failed to visualize the lesion diameter due to inadequate image resolution (Pourtaheri *et al.*, 2014; Becerra *et al.*, 1995). Najafi *et al.* (2016) used high-field magnetic resonance imaging (MRI) to track the development and enlargement of syrinxes in a rodent model of PTS obtaining high image resolution of the cavity, but failed to capture the three-dimensional (3D) morphology of the cavity; therefore, high-field MRI was deemed not sufficiently reliable to objectively perform a quantitative investigation of the morphometric cavity. To address these problems it would be ideal to employ a novel imaging technique to trace the cavity formation in a 3D manner. Currently, various phase-contrast microtomography (PCT) techniques have been developed to exploit the 3D phase-contrast information of biosamples, including propagation-based imaging, analyzer-based imaging, interferometric methods based on the use of crystals, and grating interferometric and grating non-interferometric methods (Bravin *et al.*, 2013). Among them, propagation-based synchrotron radiation microtomography (PB-SRμCT) is experimentally the simplest PCT and has no requirements of complex experimental apparatus in the light path (Bravin *et al.*, 2013; Suortti & Thomlinson, 2003). It has been regarded as an excellent 3D investigation tool for soft-tissue characterization where conventional absorption microtomography fails (Hu *et al.*, 2017; Cao *et al.*, 2017). A 3D imaging approach will undoubtedly lead to novel insights and improve our understanding of the structural adaptions that occur in various types of disease (Zhang *et al.*, 2014, 2015*a*; Cao *et al.*, 2016; Zehbe *et al.*, 2010). PB-SRμCT benefits from increased brilliance X-ray sources, which are several orders of magnitude stronger than conventional X-ray sources (Dong *et al.*, 2014), facilitating the improvement in image quality and resolution. In particular, the mapping of the phase shift of the synchrotron radiation beam allows the simultaneous exploration of the interaction between the vasculature and neuro cells and nerve fibers in biological samples (Fratini *et al.*, 2015; Hu *et al.*, 2017). Preclinical PB-SRμCT can provide 3D imaging of the microstructure and degradation changes of implanted biodegradable scaffolds after SCI (Takashima *et al.*, 2015). However, the feasibility and accuracy of PB-SRμCT for cystic cavity measurement have not been assessed. In our study, we aimed to evaluate the feasibility of PB-SRμCT in the 3D visualization of cavity formation after SCI in a rat model of PTS. Additionally, to better assess the spatial arrangement of the cavity and interaction with the vascular network, 3D volume renderings of the segmented cavity and vasculature network were simultaneous presented.

2. Materials and methods

2.1. Experimental animals and ethics statement

Adult male Sprague-Dawley rats weighing 220–250 g obtained from the Center of Experimental Animals were used in this study. All surgical interventions and perioperative care were performed in accordance with internationally accepted principles and were approved by the Animal Care and Ethics Committees of Xiangya Hospital, Central South University (Permit Number: 201703563).

2.2. Cystic cavity induction and study design

The rat model of PTS was established according to previously described methods with slight modifications (Najafi *et al.*, 2016). Briefly, the rats were intraperitoneally (i.p.) anesthetized with chloral hydrate. Afterwards, the rat skin was shaved and prepared with povidone iodine. A laminectomy was performed at thoracic vertebra level 10 (T10). Using the infinite horizon impactor (Precision Systems and Instrumentation, Lexington, KY, USA), a 75 kDyn impact was delivered to the spinal cord to produce the PTS model without causing significant neurological deficits in the animals. A 5 μl injection of 250 g ml^{-1} kaolin (Sigma-Aldrich) diluted in 0.9% saline solution was administered to the subarachnoid space with a syringe after the spinal cord injury. After surgery, the rats were housed individually in cages with free access to food and water. A pain relief drug (Tramadol; Grunenthal GmbH, Aachen, Germany) and antibiotic (penicillin sodium; North China Pharmaceutical Co, Shijiazhuang, China) were administered once daily within the first three days after surgery. The bladders were manually expressed twice daily until full voluntary or autonomic voiding was obtained. The animals were scanned ten weeks after cystic cavity induction. At the time of scanning, the animals were killed, and the spinal cord samples were isolated from the rats and were prepared for PB-SRCT scanning ($n = 10$).

2.3. PB-SRμCT scanning

PB-SRμCT scanning was performed using the BL13W1 biomedical beamline at the Shanghai Synchrotron Radiation Facility (SSRF) in China. Before PB-SRμCT examination, the rats were euthanized with an overdose of 10% chloral hydrate (6 ml kg^{-1}, i.p.). A thoracotomy was rapidly performed to expose the heart. Next, the vascular system was perfused with heparinized saline *via* the ascending aorta to facilitate rapid and sufficient draining of blood, followed by vessel network fixation with 4% paraformaldehyde in phosphate-buffered saline (PBS) using a previously described method (Hu *et al.*, 2012). Subsequently, 8 mm spinal cord segments of tissue containing the cystic cavities were post-fixed in 4% paraformaldehyde for 24 h at 4°C. All the spinal cord tissue specimens were dehydrated using a graded ethanol series and were prepared for PB-SRμCT scanning. The spinal cord samples were placed into a tube and were mounted on a rotary stage in line with the synchrotron radiation X-ray beam. The X-rays were converted to visible light by a cleaved

Lu_2SiO_5:Ce single-crystal scintillator. After the beam passed through the sample, the inner structure of the specimen was digitized by an ordinary high-resolution 2048 pixel × 2048 pixel CCD camera (pco.2000, PCO AG, Kelheim, Germany) with a physical pixel size of 3.7 µm (Fig. 1). To provide good phase-contrast information of the sample, the imaging parameters were optimized according to our previous study: the X-ray beam energy in the current experiment was set at 15 keV; the effective pixel size of the CCD detector was set at 3.7 µm; the standard field of view arising from this resolution was approximately 8 mm; the sample-to-detector distance (SDD) was adjusted to 30 cm, and the exposure time was set at 10 ms. For each acquisition, 720 projection images were captured.

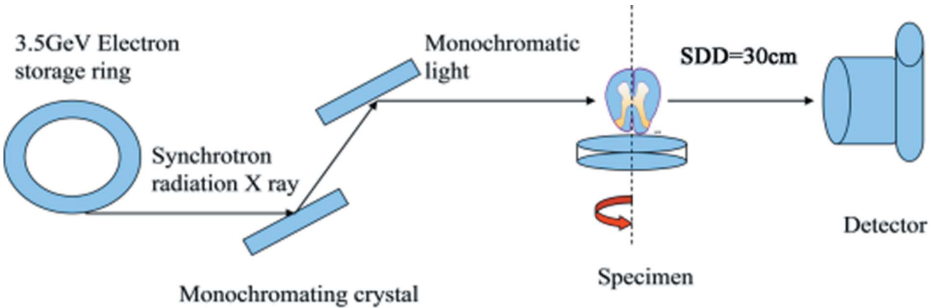

Figure 1
Schematic of the experimental setup for PB-SRµCT imaging at the BL13W1 station in SSRF. Monochromated synchrotron radiation X-rays are projected onto a sample mounted on the sample stage allowing 180° rotation to produce the projection images, and the transmitted beam is recorded by the CCD detector after the X-rays propagate a proper distance from the object.

2.4. Image processing and analysis

Total projected images were reconstructed using software developed by SSRF to perform a directly filtered back-projection algorithm (Chen *et al.*, 2014). The illuminated object can be completely described by the 3D complex refractive index distribution as follows: $n(x, y, z) = 1 - \delta(x, y, z) + i\beta(x, y, z)$, where x, y and z describe the coordinate system of the sample, δ is the refractive index decrement, related to the phase shift of the incident wave after passing through the specimen, and β is the absorption index of the sample (Bravin *et al.*, 2013). The theoretical values of β and δ were calculated with the X-ray attenuation properties model of DCM (http://research.csiro.au/dcm). The larger sample-to-detector distances increased the contrast primarily due to the contribution from differences in the refractive properties across the sample in addition to the differential absorption (Guo *et al.*, 2016; Bravin *et al.*, 2013). To enhance the quality of slice reconstruction, X-TRACT SSRF CWS x64 (Commonwealth Scientific and Industrial Research Organization, Australia) was used for phase-contrast information extraction (Murrie *et al.*, 2014, 2015; Beltran *et al.*, 2011). During phase extraction, the parameter δ/β was adjusted to 1200 according to the theoretical values. After phase retrieval and reconstruction, the calculated β values were approximately 7.30×10^{-10} and 1.10×10^{-9}, respectively. Next, the spinal cord sample range of β values in the images was truncated and rescaled to a gray value of 0–255 (8-bit gray level) (Figs. 2A–2D). The 2D slice image and 3D image of the cavity were analyzed separately. Using *Image-Pro Plus 6.0* (Media Cybernetics, USA) software, the gray-level distribution across the cavity in transverse sections, the lesion and spared tissue with an interval of 1200 µm rostral and caudal to the lesion epicenter area, were measured. In Figs. 2A–2D, a gray level of approximately 23.6 ± 2.4 represents the cavity (3, Fig. 2I), 48.7 ± 4.3 refers to spinal cord parenchyma tissue (1 and 5, Fig. 2I) and 68 ± 6.7 indicates the boundary of the cavity (2 and 4, Fig. 2I). The 3D-rendered images were visualized using *VGStudio Max* (Version 2.1; Volume Graphics GmbH, Germany) and were analyzed with the commercially available software *Image-Pro Analyzer 3D* (Version 7.0; Media Cybernetics, Inc., USA) to obtain quantitative information, including the maximum, minimum and mean diameters, as well as the volume of the cystic cavity. To calculate the size of the cavity, the spared volume of the spinal cord tissue was first segmented *via* thresholding as placement of the regions-of-interest mask. A second volume mask was then generated by a flooding algorithm to fill the inside cavity region, from which the size of the cavity was computed as the volume of the second mask.

2.5. Immunohistochemistry and histomorphometry examination

After PB-SRµCT scanning, the corresponding sample was prepared for histological assessment by immunofluorescence and hematoxylin and eosin (H&E) staining. At the time of euthanasia, the animals were perfused as described above. The same length segment of spinal cord tissue was harvested and fixed with 4% paraformaldehyde in PBS (pH 7.4) at 37°C for 2 h. Afterwards, the segments were cryoprotected with 6% sucrose in PBS and were embedded in optimal cutting temperature (OCT) compound (Sakura Finetek USA) for slicing into 10 µm-thick sections. The sections were blocked with 10% goat serum that was diluted in PBS for 1 h, followed by incubation with a mouse monoclonal anti-RECA-1 antibody (1:200; Abcam plc, Cambridge, UK) overnight at 4°C. Next, sections were incubated with an Alexa Fluor 488 goat anti-mouse IgG secondary antibody (H + L) (1:1000, Jackson ImmunoResearch, USA) for 1 h at room temperature. The sections were also stained with H&E for histological comparison. Images were captured using an Olympus BX51 microscope (Olympus America), and the mean diameter of the cavity, measured in multiple sections from each sample, was calculated using *Image-Pro Plus 6.0* (Media Cybernetics, USA) software. The morphology obtained from histological staining was compared with the results obtained from the PB-SRµCT imaging.

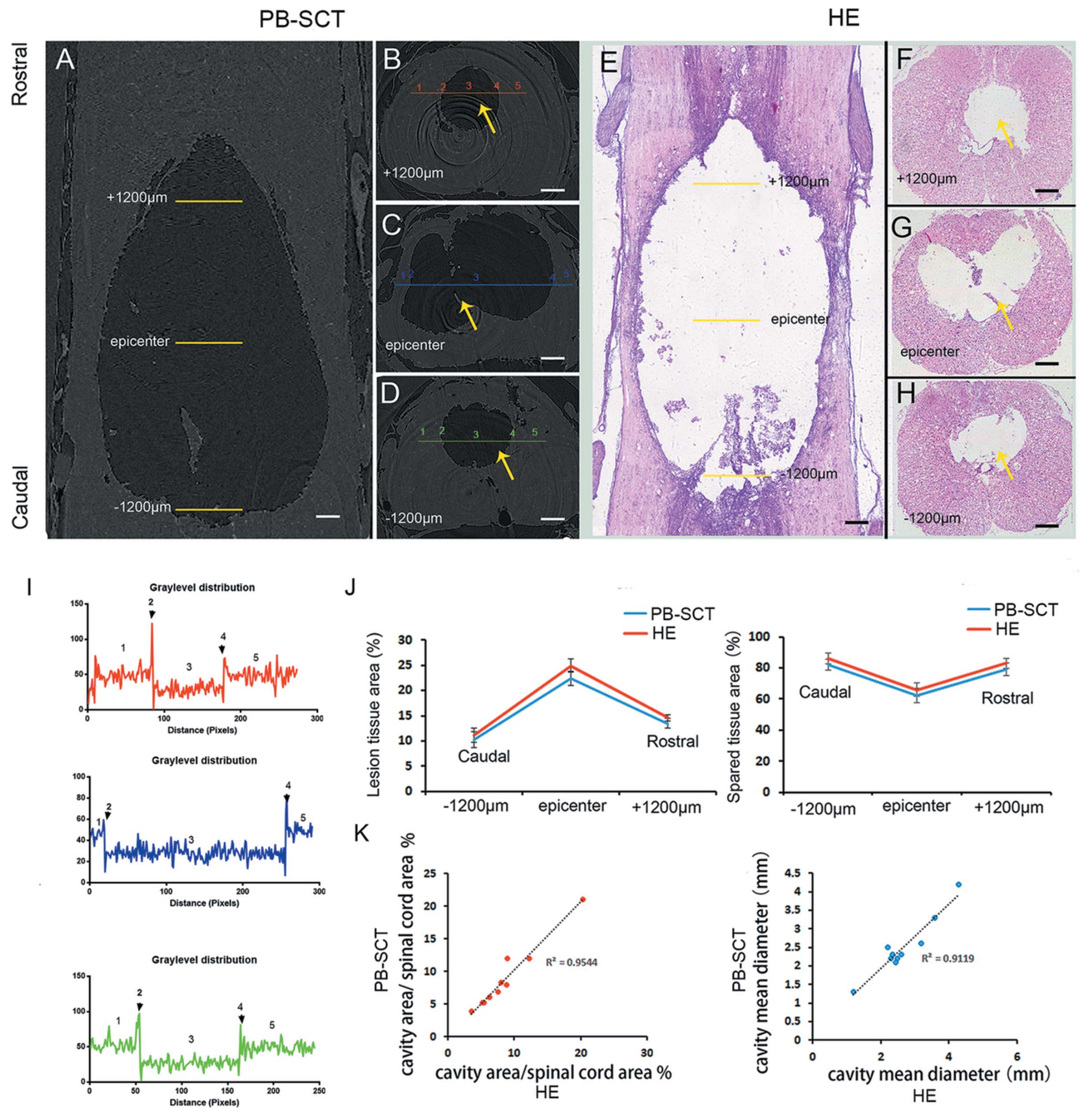

Figure 2

Correlation between PB-SRμCT and histological images in a rat model of PTS. (A–D) Sagittal and axial views of PB-SRμCT images showing a large cavity (yellow arrow). (E–H) The corresponding H&E staining images demonstrate the cord cavity. (I) The intensity profile of the corresponding line marked in (B–D) (spinal cord tissue: 1 and 5; boundary of the cavity: 2 and 5; cavity: 3). (J) Quantification of the lesion size and spared tissue within the injury site and 1200 μm distance rostral and caudal to the epicenter after cavity induction. (K) Comparison between the cavity area and mean diameter by PB-SRμCT and histological studies (r = 0.9544 and 0.9119, respectively). Scale bar = 200 μm.

2.6. Statistical analysis

All experimental data analyses were performed using IBM *SPSS Statistics*. The data values were presented as mean ± standard deviation. A paired t-test with Bonferroni adjustment was used to compare the cavity size from the PB-SRμCT images and histological sections. A p-value of less than 0.05 was interpreted to be statistically significant.

3. Results

3.1. PB-SRμCT 2D slice imaging and histopathologic observations

All animal spinal cords developed a cavity at 10 weeks post injury. PB-SRμCT yielded high-resolution sagittal and serial axial images of the rat thoracic cord cavity without significant ring artifacts (Figs. 2A–2D). Due to the lower density of the cavity than the surrounding spinal cord parenchyma tissue, the cavity appeared as a dark feature in the spinal cord tomographic image with a low gray level. Histological results indicated pathological changes in the injured spinal cord after cavity induction, including astrocyte proliferation and inflammation at the site of injury (Figs. 2E–2H). The spinal cord parenchyma was largely occupied by the cavity (yellow arrow), possibly causing mechanical pressure on the surrounding spinal cord tissue. Astroglial proliferation was also observed adjacent to the cavity and in the septa between multiple cavities (Fig. 2E). The shape and location of the cavity in the 2D PB-SRμCT slice images largely matched those in the histological sections subjected to H&E staining. As shown in Fig. 2I, the intensity profile of the corresponding line marked in Figs. 2B, 2C and 2D displayed the distribution in the gray level between the cavity and spinal cord tissue. The gray level in the cavity (3, Fig. 2I) was lower than that in the spinal cord tissue (1 and 5, Fig. 2I), and the boundary of the cavity showed a sudden change in pixel intensity between the spared spinal cord tissue and cavity (2 and 4, Fig. 2I). The calculated lesion tissue area and spared tissue area as a percentage of the intact spinal cord area at the serial level of injury site in the PB-SRμCT 2D slice image were similar to those from histological sections. No significant difference was detected between these two methods ($p > 0.05$) (Fig. 2J). The calculated cavity area as a percentage of the spinal cord area from the PB-SRμCT image correlated well with that from histological measurements [Pearson correlation coefficient (r) = 0.9544]. The cavity mean diameter from PB-SRμCT and histology also correlated well (r = 0.9119) (Fig. 2K).

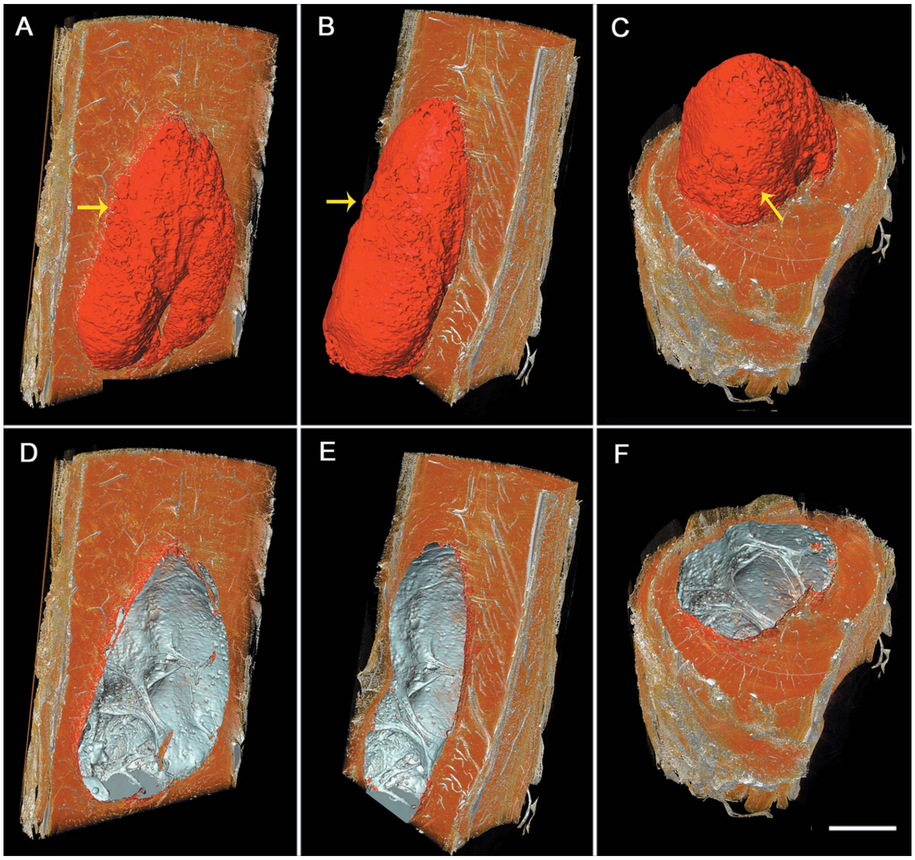

Figure 3
3D morphology of the cord cavity. (A, B, C) Sagittal, coronal and axial views of the segmented cavity (yellow arrow) within the spinal cord. (D, E, F) Inner structure of the cavity from multiple perspectives. Scale bar = 500 μm.

3.2. 3D visualization of the cavity

Figs. 3A, 3B and 3C show the sagittal, coronal and axial views of the segmented cavity, respectively, marked with red within the surrounding spinal cord tissue. The cavity was deep in the spinal cord parenchyma. To better visualize the cavity, we used a red color-coding system to label the virtual sections. Using this method, the inner structure of the 3D morphology of the cavity in the spinal cord was vividly depicted from multiple perspectives (Figs. 3D, 3E and 3F). Fig. 4A shows a representative high-resolution image of the inner feature of the cavity. As shown in Figs. 4B and 4C, the local detail of the cavity demonstrated the 3D morphology of the observed septa possessing a criss-crossing structure. The quantitative morphological data of the cavity are listed in Fig. 4D. The maximum and minimum diameters and the volume of the cavity varied among the ten samples. The mean maximum and minimum lengths of the cavity were 1.487 ± 0.017 mm and 2.93 ± 0.389 mm, respectively, and the average volume was 4.88 ± 0.842 mm^3 (Fig. 4D).

3.3. Simultaneous detection of the 3D cavity and microvasculature network

To better visualize the interaction of the vascular arrangement and relationship to the cavity, the intensity-based segmentation approach was used to reconstruct the 3D morphology of the cavity and vasculature network. After applying this method, a 3D rendering of the cavity and microvasculature can be simultaneously and vividly depicted. An example according to two different viewing angles is shown in Figs. 5A and 5B. The smallest visible vessels were approximately 10 μm in diameter. The blood vessels were adjacent to the cavity and no vessel was visualized in the cavity from the 3D view obtained by PB-SRμCT. This was confirmed by the images shown in Figs. 5C and 5D, which are based on vessel immunofluorescence staining.

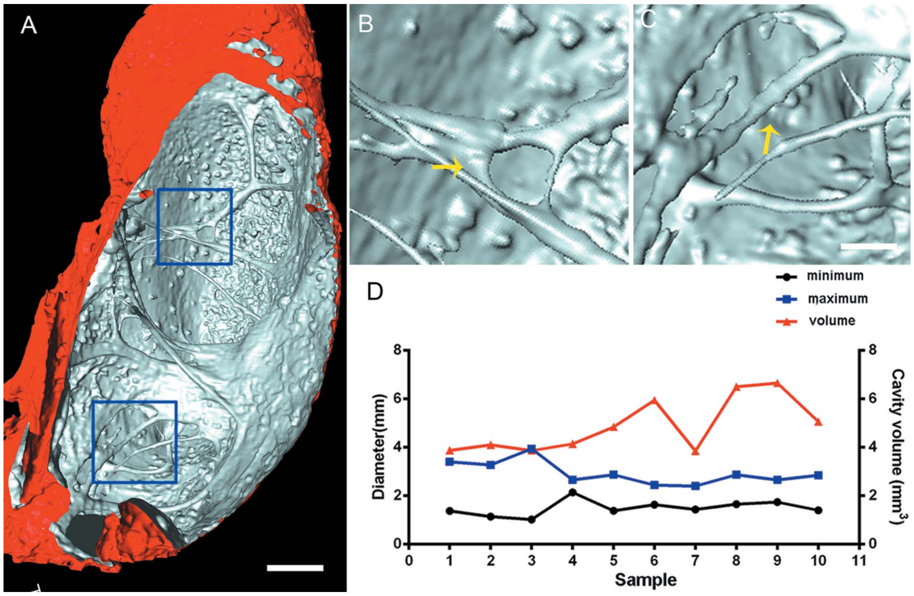

Figure 4
3D morphology of the cavity and quantitative data. (A) Representative 3D image of a cavity within the spinal cord. (B, C) Local details of the septa (yellow arrow) are detected in 3D within the inner structure of the cavity. (D) Distribution of the minimum and maximum diameters, as well as the volume of the cord cavity, among the ten samples. A: scale bar = 500 µm; B and C: scale bar = 50 µm.

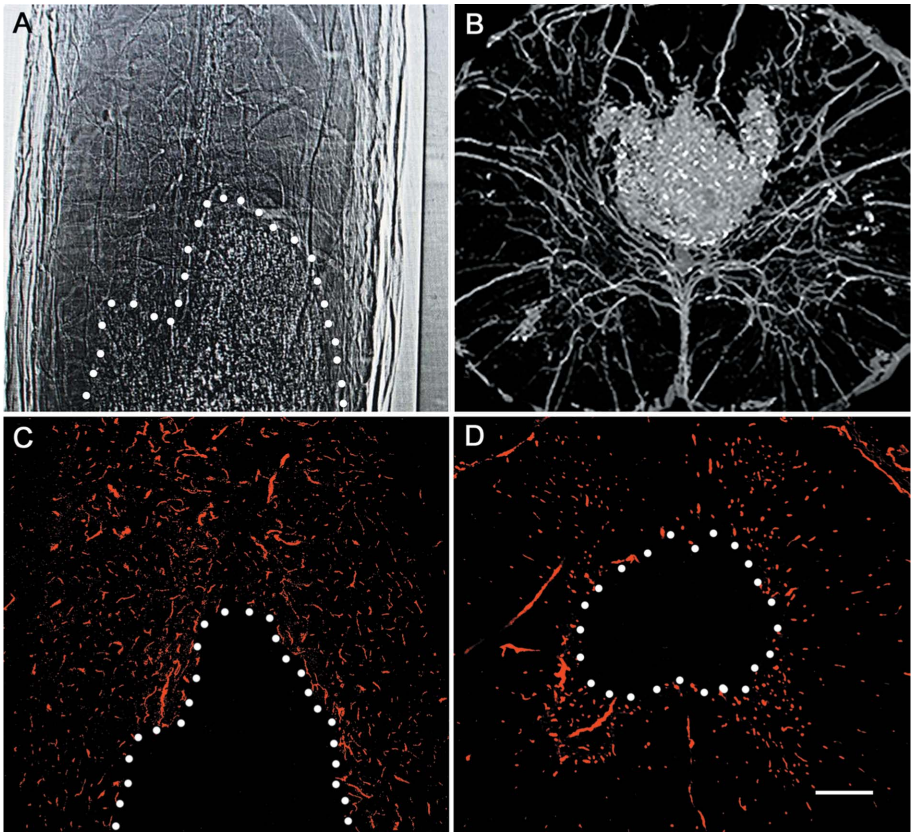

Figure 5
3D morphology of the cavity and surrounding microvasculature networks. (A, B) Sagittal and axial views of PB-SRµCT images demonstrated that the 3D morphology of the cavity (dotted line) and relationship with the vasculature correlate well with the immunofluorescence images (C, D). Scale bar = 100 µm.

4. Discussion

In this paper, we have demonstrated that PB-SRµCT can clearly depict the 3D morphology of the cavity and microvasculature network simultaneously surrounding the cavity in a rat model of PTS. Furthermore, the PB-SRµCT image was largely consistent with the morphology observed *via* the histological method. In addition, the 3D shape and quantitative parameters of the cavity based on PB-SRµCT were reported for the first time. Cavity formation within the spinal cord is common after traumatic SCI. The cavity could cause further damage to the spinal cord and impair neurological function (Burchiel, 1986). In PTS, cavity formation is followed by extension and enlargement of the cystic cavity. Although many histopathological descriptions of trauma-induced syringomyelia have been reported previously (Brodbelt *et al.*, 2003*a*,*b*), the pathophysiology of PTS is not fully understood. Cystic cavities have 3D features and are deeply located in the spinal cord parenchyma, making it challenging to visualize and quantify the 3D features of a cystic cavity using conventional imaging techniques (Wong *et al.*, 2016; Najafi *et al.*, 2016). However, the observation of an injured spinal cord with an intact cavity enables the accurate calculation of cavity size and monitoring of the changes induced by trauma. These abilities will be beneficial for the further study of the pathological processes of PTS and development of effective therapies. *In vivo* or *ex vivo* MRI is considered the gold standard for the imaging of acute SCI and for PTS detection (Najafi *et al.*, 2016; Zhang *et al.*, 2015*b*). However, MRI analysis also has its own limitations. In previous studies, researchers have reported that the cavity could not be measured due to inadequate resolution. Additionally, MRI provides a 2D image of the cavity (Becerra *et al.*, 1995; Najafi *et al.*, 2016). A better solution with higher image resolution is diffusion tensor imaging (DTI), which has been reported to provide more accurate quantitative information about the lesion area; however, DTI generally shows very low signal intensity compared with MRI (Jirjis *et al.*, 2013). Scanning electron microscopy has been demonstrated to serve as a promising tool and provides high-resolution in-depth images for tissue characterization; however, this technique requires physical destruction of the sample (Koyanagi *et al.*, 1993). Currently, the development of a 3D imaging technique to evaluate the cavity size and location has attracted great attention. In our study, computed tomography (CT) coupled with PB-syncing has been employed for cavity 3D visualization. This technique has recently been reported to serve as a powerful imaging technique to visualize the micro- and ultrastructure of soft tissue (Zehbe *et al.*, 2010). In addition to the high-resolution qualitative visualization of 3D features, PB-SRμCT allows accurate and direct 3D measurement within the structure of the sample. To our knowledge, this is the first study to evaluate high-resolution 3D images in a rodent model of PTS using PB-SRμCT and to provide quantitative information of a cystic cavity. Furthermore, the small cavity and spinal cord vessel network are simultaneously detected in 3D. In a study by Najafi *et al.* (2016), the cavity volume was quantified by manually tracing and calculating the axial MRI images using *ImageJ* software. This technique is very time-consuming and requires significant user interaction. Due to the low imaging resolution of MRI, the measurements based on the MRI images are likely inaccurate, potentially introducing bias into the results. In our study, an automated segment toolkit based on the phase-contrast information included in the *Image-Pro Analyzer 3D* software was directly used to calculate the 3D shape of a cavity; this method has previously been conducted for the 3D profiling of the mixing and segregation of granules (Yin *et al.*, 2016).

The well delineated characteristics of the low gray-value region on 2D PB-SRμCT slice images largely matched the cavities observed using the histological method, and this agreement validated the accuracy of the PB-SRμCT method. Additionally, we found no blood vessels in the cavity, and tissue loss was primarily located in the center of the spinal cord parenchyma. The cavity volume was not confined to the injury but was rather extended rostrally and caudally. This observation could explain the expansion of syringomyelia, which can cause damage around the cavity and can result in the progressive loss of sensory or motor function. The septa divided the cavity into several small spaces, as visualized both in the 2D and 3D PB-SRμCT images. By applying segment thresholding on the reconstructed image, the 3D morphology of the cavity could be well depicted without tissue sectioning, a phenomenon that is also important and provides further insight into the pathophysiology of the disease. In this study, all animal spinal cords developed a cavity, but the maximum and minimum diameters and volumes of the cavities varied among the ten samples. The morphologic diversity may be due to minor differences in establishing the animal model during the procedure that are difficult to prevent. Because our results provided quantitative 3D features of the cavity using PB-SRμCT that were more accurate than the morphological characteristics obtained from 2D images, these data have great potential to better understand the actual properties of cystic cavity formation in the spinal cord injury of patients with PTS.

There are several limitations in our study. First, one advantage of MRI is that it can be used *in vivo*. The technique used in this study was *ex vivo* scanning. The technical complications have limited the implementation of *in vivo* imaging in studies of the 3D morphology of the cavity in the living rat spinal cord. The longitudinal measurement of syrinx size *in vivo* is impossible with this technique. In particular, the anatomical proximity of the spinal cord to the heart generates significant movement artifacts, making 3D reconstruction of the living spinal cord fail. Additionally, in the production of high-resolution images, the image field tends to be small. Therefore, the region of interest for *in vivo* scanning must be smaller to be contained in the imaging field. However, we still believe that our imaging method, which provides the 3D morphology and quantitative features of the cavity, will be beneficial for future research because there are scant published data on the 3D visualization of a cystic cavity. Finally, the cavities imaged in the current study may not accurately represent the *in vivo* situation in which the cerebrospinal fluid circulation is intact, and the high pressure within the cavity likely compresses the surrounding tissue. It is likely that the euthanasia of an animal leads to a decrease in the size of the cavity in the absence of these high pressures. In future studies, we plan to perform *in vivo* imaging to simultaneously monitor cavity formation and provide more accurate information regarding the progressive changes in the cavity over an extended period once the challenges are well resolved.

In summary, in this study we demonstrated that *ex vivo* PB-SRμCT can vividly depict the 3D morphology of a cavity and surrounding microvasculature. The 3D morphological parameters of the cavity based on this method provide more valuable information and contribute to future PTS studies. Therefore, PB-SRμCT has great potential and will serve as a powerful *ex vivo* 3D imaging technique to understand central nervous system-related disorders in preclinical models and will provide reliable qualitative and quantitative data for disease characterization.

Acknowledgements

This work was performed at the SSRF BL13W1, Shanghai, China. We thank Professor Tiqiao Xiao and staff for their kind assistance in PB-SRμCT measurements at the BL13W1 station.

Funding information

The following funding is acknowledged: National Natural Science Foundation of China (award No. 81301542, 81371956, 81171698 and 61772556); Fundamental Research Funds for the Central Universities of Central South University (award No. 2016zzts123); Hunan Provincial Innovation Foundation For Postgraduate (award No. CX2015B060).

References

Asano, M., Fujiwara, K., Yonenobu, K. & Hiroshima, K. (1996). *Spine*, **21**, 1446–1453.

Becerra, J. L., Puckett, W. R., Hiester, E. D., Quencer, R. M., Marcillo, A. E., Post, M. J. & Bunge, R. P. (1995). *Am. J. Neuroradiol.* **16**, 125–133.

Beltran, M. A., Paganin, D. M., Siu, K. K., Fouras, A., Hooper, S. B., Reser, D. H. & Kitchen, M. J. (2011). *Phys. Med. Biol.* **56**, 7353–7369.

Bilston, L. E., Stoodley, M. A. & Fletcher, D. F. (2010). *J. Neurosurg.* **112**, 808–813.

Bravin, A., Coan, P. & Suortti, P. (2013). *Phys. Med. Biol.* **58**, R1–R35.

Brodbelt, A. R., Stoodley, M. A., Watling, A. M., Tu, J., Burke, S. & Jones, N. R. (2003*b*). *Spine*, **28**, E413–E419.

Brodbelt, A. R., Stoodley, M. A., Watling, A. M., Tu, J. & Jones, N. R. (2003*a*). *Eur. Spine J.* **12**, 300–306.

Burchiel, K. (1986). *West. J. Med.* **145**, 84–85.

Cao, Y., Liao, S., Zeng, H., Ni, S., Tintani, F., Hao, Y., Wang, L., Wu, T., Lu, H., Duan, C. & Hu, J. (2017). *Sci. Rep.* **7**, 43094.

Cao, Y., Zhang, Y., Yin, X., Lu, H., Hu, J. & Duan, C. (2016). *Sci. Rep.* **6**, 21838.

Chen, R., Liu, P., Xiao, T. & Xu, L. X. (2014). *Adv. Mater.* **26**, 7688–7691.

Dong, P., Haupert, S., Hesse, B., Langer, M., Gouttenoire, P. J., Bousson, V. & Peyrin, F. (2014). *Bone*, **60**, 172–185.

Fratini, M., Bukreeva, I., Campi, G., Brun, F., Tromba, G., Modregger, P., Bucci, D., Battaglia, G., Spanò, R., Mastrogiacomo, M., Requardt, H., Giove, F., Bravin, A. & Cedola, A. (2015). *Sci. Rep.* **5**, 8514.

Guo, Z., Yin, X., Liu, C., Wu, L., Zhu, W., Shao, Q., York, P., Patterson, L. & Zhang, J. (2016). *Int. J. Pharm.* **499**, 47–57.

Hu, J., Li, P., Yin, X., Wu, T., Cao, Y., Yang, Z., Jiang, L., Hu, S. & Lu, H. (2017). *J. Synchrotron Rad.* **24**, 482–489.

Hu, J. Z., Wu, T. D., Zeng, L., Liu, H. Q., He, Y., Du, G. H. & Lu, H. B. (2012). *Phys. Med. Biol.* **57**, N55–N63.

Jirjis, M. B., Kurpad, S. N. & Schmit, B. D. (2013). *J. Neurotrauma*, **30**, 1577–1586.

Ko, H. Y., Kim, W., Kim, S. Y., Shin, M. J., Cha, Y. S., Chang, J. H. & Shin, Y. B. (2012). *Spinal Cord*, **50**, 695–698.

Kobayashi, S., Kato, K., Rodríguez Guerrero, A., Baba, H. & Yoshizawa, H. (2012). *J. Neurotrauma*, **29**, 1803–1816.

Koyanagi, I., Tator, C. H. & Lea, P. J. (1993). *Neurosurgery*, **33**, 285–291; discussion 292.

Krebs, J., Koch, H. G., Hartmann, K. & Frotzler, A. (2016). *Spinal Cord*, **54**, 463–466.

Murrie, R. P., Morgan, K. S., Maksimenko, A., Fouras, A., Paganin, D. M., Hall, C., Siu, K. K. W., Parsons, D. W. & Donnelley, M. (2015). *J. Synchrotron Rad.* **22**, 1049–1055.

Murrie, R. P., Stevenson, A. W., Morgan, K. S., Fouras, A., Paganin, D. M. & Siu, K. K. W. (2014). *J. Synchrotron Rad.* **21**, 430–445.

Najafi, E., Bilston, L. E., Song, X., Bongers, A., Stoodley, M. A., Cheng, S. & Hemley, S. J. (2016). *J. Neurosurg. Spine*, **24**, 941–948.

Pourtaheri, S., Emami, A., Sinha, K., Faloon, M., Hwang, K., Shafa, E. & Holmes, L. Jr (2014). *Spine J.* **14**, 2546–2553.

Shields, C. B., Zhang, Y. P. & Shields, L. B. (2012). *Handb. Clin. Neurol.* **109**, 355–367.

Suortti, P. & Thomlinson, W. (2003). *Phys. Med. Biol.* **48**, R1–R35.

Takashima, K., Hoshino, M., Uesugi, K., Yagi, N., Matsuda, S., Nakahira, A., Osumi, N., Kohzuki, M. & Onodera, H. (2015). *J. Synchrotron Rad.* **22**, 136–142.

Tu, J., Liao, J., Stoodley, M. A. & Cunningham, A. M. (2011). *J. Neurosurg. Spine*, **14**, 573–582.

Wong, J. H., Song, X., Hemley, S. J., Bilston, L. E., Cheng, S. & Stoodley, M. A. (2016). *J. Neurosurg. Spine*, **24**, 797–805.

Yin, X. Z., Wu, L., Li, Y., Guo, T., Li, H. Y., Xiao, T. Q., York, P., Nangia, A., Gui, S. Y. & Zhang, J. W. (2016). *Sci. Rep.* **6**, 21770.

Zehbe, R., Haibel, A., Riesemeier, H., Gross, U., Kirkpatrick, C. J., Schubert, H. & Brochhausen, C. (2010). *J. R. Soc. Interface*, **7**, 49–59.

Zhang, C., Morozova, A. Y., Abakumov, M. A., Gubsky, I. L., Douglas, P., Feng, S., Bryukhovetskiy, A. S. & Chekhonin, V. P. (2015*b*). *Med. Sci. Monit.* **21**, 3179–3185.

Zhang, J., Zhou, G., Tian, D., Lin, R., Peng, G. & Su, M. (2015*a*). *Sci. Rep.* **5**, 13831.

Zhang, M. Q., Sun, D. N., Xie, Y. Y., Peng, G. Y., Xia, J., Long, H. Y. & Xiao, B. (2014). *Br. J. Radiol.* **87**, 20130670.